Ab initio phasing of 3-dimensional partially coherent diffraction patterns.

J. N. Clark[1,*], X. Huang[1], R. Harder[2] & I. K. Robinson[1,3]

[1]*London Centre for Nanotechnology, University College, London WC1E 6BT, UK*

[2]*Advanced Photon Source, Argonne, IL 60439, USA*

[3]*Research Complex at Harwell, Didcot, Oxfordshire OX11 0DE, UK*

Ever since Thomas Young demonstrated interference effects of light with his famous double-slit experiment, there has been intense interest in understanding its wave nature. An intense area of research has focussed on determining the interference properties of the light wavefield via its coherence properties, which play an important role in imaging applications. One imaging technique that has experienced rapid growth is coherent diffractive imaging (CDI) [1–5]. CDI recovers an object from its diffraction pattern with the potential of wavelength-limited resolution. A critical requirement of the method is that the illumination is coherent. Diminished coherence results in reconstructions that suffer from artefacts or fail completely [6–9]. In this letter we demonstrate *ab initio* phasing of partially coherent diffraction patterns in 3 dimensions by recovering the complex density of a gold nanocrystal whilst simultaneously determining the coherence properties of the illuminating wavefield. This has broad implications for both CDI and wavefield characterisation with x-rays, electrons and lab-based x-ray sources [10].

CDI offers great opportunities to image a wide variety of samples [1–4] in 2- and 3-dimensions

[5,8] with atomic and sub-atomic resolution [3,11]. CDI works by illuminating a sample with a coherent wavefield after which the coherent diffraction pattern is recorded. The missing phase of the diffracted wave is retrieved through iterative [12] or single step methods [13]. The CDI method requires that the wavefield emanating from the object be isolated. Isolation of the object ensures that a minimum sampling requirement is met [14] when the diffracted intensity is recorded. If the sample is not sufficiently isolated, the illuminating wavefield can be used to define the extent of the sample [15] while using overlap between adjacent positions facilitates imaging of extended objects [16]. Essential for CDI is the requirement that the illuminating wavefield is coherent. By performing CDI with visible laser light or an x-ray free electron laser ensures this requirement is closely met. However, many CDI experiments use 3rd generation synchrotron or electron sources which can be far from fully coherent [17,18]. Consequently, there has been recent progress in adapting the current algorithms to accommodate both spatial [6] and temporal [19,20] partial coherence. Until now these methods have been limited to 2 dimensions with complete *a priori* knowledge of the coherence properties of the illumination.

Under the far-field approximation, the diffracted intensity, $I(\boldsymbol{q})$ from a sample's complex electron density, $\rho(\boldsymbol{r})$, is given by

$$I(\boldsymbol{q}) = \int\int \Gamma(\boldsymbol{r}_1, \boldsymbol{r}_2, \tau)\rho(\boldsymbol{r}_1)\rho^*(\boldsymbol{r}_2)\exp\left[i2\pi\boldsymbol{q}\cdot(\boldsymbol{r}_1-\boldsymbol{r}_2)\right]\mathrm{d}\boldsymbol{r}_1\mathrm{d}\boldsymbol{r}_2 \tag{1}$$

$$= |\hat{\psi}(\boldsymbol{q})|^2, \tag{2}$$

where $\boldsymbol{r}$ is a sample space co-ordinate, $\boldsymbol{q}$ is a reciprocal space coordinate, $\hat{\psi}$ is the complex scalar diffracted wavefield given by, $\hat{\psi}(\boldsymbol{q}) = |\hat{\psi}(\boldsymbol{q})|\exp\left[i\phi(\boldsymbol{q})\right]$ and $\Gamma(\boldsymbol{r}_1, \boldsymbol{r}_2, \tau)$ is the mutual coherence

function (MCF) of the illumination. Iterative algorithms are used to recover the phase of $\hat{\psi}$ by enforcing constraints in the detector and sample plane. The first of the two more common constraints is the modulus constraint, which requires that the modulus of the wavefield at the detector agrees with that measured (from its intensity). The second constraint is the support constraint, which assumes *a priori* that the sample is finite in extent. Ensuring that there is a sufficient no-density region surrounding the sample ensures that under ideal conditions (*i.e.*, noiseless) the recovered object is unique [21] for dimensions of 2 or more (aside from the "trivial solutions" such as conjugation and reflection). The MCF for partially coherent illumination is given by,

$$\Gamma(\boldsymbol{r}_1, \boldsymbol{r}_2, \tau) = J(\boldsymbol{r}_1, \boldsymbol{r}_2)\gamma(\tau), \tag{3}$$

where $\gamma(\tau)$ is the normalised temporal MCF and

$$J(\boldsymbol{r}_1, \boldsymbol{r}_2) = \psi_i(\boldsymbol{r}_1)\psi_i^*(\boldsymbol{r}_2)\gamma(\boldsymbol{r}_2 - \boldsymbol{r}_1), \tag{4}$$

is the mutual optical intensity (MOI) described by the generalised-Schell model [22], ψ_i is the illuminating wavefield and $\gamma(\boldsymbol{r}_2 - \boldsymbol{r}_1)$ is the normalised spatial MCF. The recorded intensity is now given by [9,23],

$$I_{pc}(\boldsymbol{q}) = I_c(\boldsymbol{q}) \otimes \hat{\gamma}(\boldsymbol{q}), \tag{5}$$

where $\hat{\gamma}(\boldsymbol{q})$ is the Fourier transform of the normalised MCF. The normalised MCF can be written so that $\gamma(\boldsymbol{x}) = \gamma(\boldsymbol{x}_\perp)\gamma(\boldsymbol{x}_\parallel)$ where $\boldsymbol{x} = \boldsymbol{r}_2 - \boldsymbol{r}_1$ with $\boldsymbol{x}_\perp$ and $\boldsymbol{x}_\parallel$ representing the directions transverse and along the beam direction respectively with a change from the time domain to the longitudinal direction for the normalised temporal MCF. The transverse coherence properties are embodied in

$\gamma(\boldsymbol{x}_\perp)$ and the temporal (or longitudinal) coherence properties relating to the monochromaticity of the wavefield are embodied in $\gamma(\boldsymbol{x}_\parallel)$.

The effect of Eq. 5 is to blur the coherent intensity by convolving it with the Fourier transform of the normalised MCF [9,23]. The partially coherent diffraction pattern is no longer the modulus of the diffracted wavefield which results in there being no object that will simultaneously satisfy the modulus and support constraints [7,17]. Depending on the degree of degradation, the iterative algorithms can produce reconstructions that contain artefacts, non-unique solutions or fail to converge at all [6–9]. As a consequence, we have developed a modified iterative algorithm that allows successful inversion of partially coherent diffraction patterns whilst simultaneously recovering coherence properties of the illuminating wavefield without assumption about *a priori* form in 3-dimensions.

To demonstrate simultaneous recovery of a sample and the normalised MCF of the illumination from 3-dimensional diffraction data (Fig. 1), an experiment was carried out at beamline 34-ID-C at the Advanced Photon Source in Chicago (see Methods). The sample consisted of Au nano-crystals several hundred nanometers in diameter (see Methods). In order to accommodate partial coherence the modulus constraint needs to be modified. Modification of the modulus constraint has proven successful in accommodating partial temporal [19,20] and spatial [6] coherence using modal techniques. The modal methods assume the recorded diffraction is made up of a number of modes, with the estimate at the recorded diffraction being the incoherent sum of each modes intensity. Other modifications of the modulus constraint have successfully been incorporated for

dynamic sample imaging [24] and molecular damage from X-ray free electron lasers [25]. Ten reconstructions were carried out for each of the slit settings, each starting with a random phase for the wavefield at the detector. All reconstructions used the same recipe which consisted of 10 iterations of Error Reduction (ER) [12] then 160 iterations of Hybrid Input-Output (HIO) [12] using $\beta = 0.9$ then 40 iterations of ER. The support was updated every fifth iteration using shrink-wrap [26]. For each of the random starts; two reconstructions were carried out, the first used the usual modulus constraint and the second used the modified modulus constraint given by Eq. 6 and Eq. 7. $\hat{\gamma}^k(\boldsymbol{q})$ was updated every 15 iterations using the iterative Richardson-Lucy algorithm (see Methods). Updating $\hat{\gamma}^k(\boldsymbol{q})$ can be performed in a number of ways. Previous methods [24,27] have used a Gaussian model for $\hat{\gamma}^k(\boldsymbol{q}, \boldsymbol{\sigma})$ and minimised $E = \int \left| I_{pc}(\boldsymbol{q}) - I^k(\boldsymbol{q}) \otimes \hat{\gamma}^k(\boldsymbol{q}, \boldsymbol{\sigma}) \right| \mathrm{d}\boldsymbol{q}$ with respect to the model parameters $\boldsymbol{\sigma}$. In the limit of full coherence, $\gamma \rightarrow \delta$ and Eq. 7 becomes the usual modulus constraint which sets the amplitude of the iterate to square root of the measured intensity while retaining the phase. It should be noted that in this framework algorithms can be developed that connect seemingly unrelated reconstruction's through a common MCF.

Figure 2 shows a typical reconstructed image of the gold nanocrystal comparing the amplitude (shown as an isosurface at 50% of the maximum) for the high (a and b) and low coherence (c and d) data sets assuming perfect coherence (a and c) and accommodating partial coherence (b and c). It is quite clear that, without correcting for the partial coherence, the reconstructed image suffers from significant unphysical density modulations, manifesting itself as a missing segment at the contour level shown (c). On the other hand, the reconstruction accommodating the partial coherence (d) represents the expected shape for a defect free nano-crystal of uniform density. This

is also in agreement with the high coherence reconstruction (a and b). Shown in Fig. 3 are transparent isosurfaces of the recovered amplitude. Such variations in density have been reported before [2,8,9,28] with the high-density regions being labelled as 'hot spots'. The hot spots were attributed to partial coherence effects due to beamline window placement [9]. The coherence corrected images (b and d) show a much more uniform interior with a well faceted crystal shape compared with those assuming full coherence (a and c). Shown in Fig. 4 are histograms of the reconstructed amplitude for points within the crystal. The low coherence histogram (c) has a significantly broader distribution of values compared with the high coherence (a) and corrected cases (b and d). A Gaussian was fitted to the histogram of the amplitude values. The standard deviation of the distribution improved by a factor of 2.7 and 3.9 for the high and low coherence reconstructions respectively after using the partially coherent modulus constraint. Importantly, these results also show us that significant improvements can be made even to the high coherence data by incorporating a partially coherent modulus constraint. We attribute this to the fact the longitudinal coherence was the same for both data sets. The resolution of the final images was estimated by fitting an error function to the edge of the reconstructed nanocrystal. The resolution was 17 nm, 8 nm and 14 nm for x, y and z directions respectively. A second nano-crystal was studied and found to show the same improvement, as presented in the suplementary information. The improvements are found to be fully three dimensional, as can be seen in the movie S1.

The full 3 dimensional normalised MCF is also recovered. Line-outs, averaged from 10 random starts, for the horizontal (x) and longitudinal (z) normalised MCF are shown in Fig. 5 along with a 2 dimensional x-z slice for the low coherence data set. The horizontal coherence

length, which can be read off as a characteristic width of these distributions is 220 nm (defined as the half-width at half maximum (HWHM) of $|\gamma|$). This compares well with the value range of 200-300 nm estimated from the beamline geometry (see supplementary information). The recovered longitudinal HWHM is 485 nm which compares well with a previously measured [28] HWHM of 660 nm for the same beamline. It is also seen that the HWHM of the horizontal coherence function increases by approximately 60$\%$ from the low (blue line) to the high (red line) coherence data set (Fig. 5 a.). There is excellent agreement between the recovered longitudinal normalised MCF from the low (red line) and high (blue line) coherence data sets (Fig. 5 b.). We note that no *a priori* form or model was assumed in this analysis. The beamline optics will largely predict the coherence properties of the illumination. Our result shows we can obtain an estimate of the coherence properties of the wavefield whilst simultaneously reconstructing an image of the sample.

The method proposed and demonstrated experimentally here has broad implications for CDI as it allows objects to be reconstructed to high resolution in 3-dimensions when their diffraction patterns have been recorded under less than ideal spatial and/or temporal coherence. This should allow considerable extension of CDI to less perfect X-ray and electron sources. It has the additional benefit of recovering coherence properties of the illumination without the need for *a priori* information. We note this has not been achieved by any other method before to this level of detail. It is anticipated that the proposed algorithm will find widespread use in CDI for high-resolution 3 dimensional imaging of biological and materials science samples from synchrotron and lab based x-ray sources as well as electron sources.

Methods

Sample preparation. To make the nano-crystals, a 2 nm layer of Ti was deposited using thermal evaporation onto an Si wafer followed by 20 nm of Au. The thin film was then annealed in air at 1000°C for approximately 10 hours after which time the film had de-wetted and formed nano-crystals.

Experiment. The sample was placed on a diffractometer and illuminated by 8.9 keV x-rays. To record the diffraction from the nano-crystals a 1350×1300 pixel CCD detector with 22.5 μm square pixels was placed 550 mm from the crystal centred about one of the (111) Bragg peaks. A set of Kirkpatrick-Baez (KB) mirrors with focal lengths of 100 mm and 200 mm in the horizontal and vertical directions respectively were used to focus the illumination onto the sample. Approximately 600 mm in front of the sample, roller blade slits were used to aperture the x-ray wavefield in the horizontal direction. Opening and closing the roller blade slits allowed adjustment of the MOI incident on the KB mirrors. To record the 3-dimensional diffraction pattern, the nano-crystals were rocked in 50 0.02° degree steps with each frame exposed for approximately 16 seconds. Data were recorded at two different roller blade slit settings, 12.5 and 50 μm, chosen to achieve the horizontally "coherent" and "partially coherent" illumination conditions respectively. Figure 1 shows lineouts taken through the 3 dimensional recorded intensity. Degradation in fringe visibility is clearly visible in the horizontal (q_x) direction only.

Phase retrieval algorithm. In order to accommodate partial coherence and simultaneously determine the coherence function, the algorithm is as follows:

1. At iteration k, given $\psi^k(\boldsymbol{r})$ propagate to the detector plane to obtain $\hat{\psi}^k(\boldsymbol{q})$.

2. Update $\hat{\gamma}^k(\boldsymbol{q})$ and then form the current estimate of the measured partially coherent data $I^k_{pc}(\boldsymbol{q})$:

$$I^k_{pc}(\boldsymbol{q}) = I^k(\boldsymbol{q}) \otimes \hat{\gamma}^k(\boldsymbol{q}), \tag{6}$$

   where $I^k(\boldsymbol{q}) = |\hat{\psi}^k(\boldsymbol{q})|^2$.

3. Apply the modulus constraint to $\hat{\psi}^k(\boldsymbol{q})$, using the measured data $I_{pc}(\boldsymbol{q})$:

$$\hat{\psi}^{k'}(\boldsymbol{q}) = \hat{\psi}^k(\boldsymbol{q}) \left(\frac{\sqrt{I}_{pc}(\boldsymbol{q})}{\sqrt{I}^k_{pc}(\boldsymbol{q})} \right). \tag{7}$$

4. Propagate $\hat{\psi}^{k'}(\boldsymbol{q})$ to the sample plane.

5. Enforce real space constraints, form the next iterate and proceed to step 1.

The iterative Richardson-Lucy (RL) algorithm [29,30] was employed to update a numerical estimate of $\hat{\gamma}^k(\boldsymbol{q})$ using the measured intensity, $I_{pc}(\boldsymbol{q})$, and the current iterates estimate of the coherent intensity, $I^k(\boldsymbol{q})$ where $\hat{\gamma}^k(\boldsymbol{q})$ is given by,

$$\hat{\gamma}^{k,i+1}(\boldsymbol{q}) = \hat{\gamma}^{k,i}(\boldsymbol{q}) \left(I^k(-\boldsymbol{q}) \otimes \frac{I_{pc}(\boldsymbol{q})}{I^k(\boldsymbol{q}) \otimes \hat{\gamma}^{k,i}(\boldsymbol{q})} \right), \tag{8}$$

where i is the sub iteration number relating to the coherence function determination. The coherence function was updated every 15 iterations with the RL algorithm typically run for no more than 50 iterations per update.

1. Miao, J., Charalambous, P., Kirz, J. & Sayre, D. Extending the methodology of x-ray crystallography to allow imaging of micrometre-sized non-crystalline specimens. *Nature* **400**, 342 (1999).

2. Robinson, I. K., Vartanyants, I. A., Williams, G. J., Pfeifer, M. A. & Pitney, J. A. Reconstruction of the shapes of gold nanocrystals using coherent x-ray diffraction. *Phys. Rev. Lett.* **87**, 195505 (2001).

3. Zuo, J. M., Vartanyants, I., Gao, M., Zhang, R. & Nagahara, L. A. Atomic resolution imaging of a carbon nanotube from diffraction intensities. *Science* **300**, 1419–1421 (2003).

4. Shapiro, D. *et al.* Biological imaging by soft x-ray diffraction microscopy. *Proc. Natl. Acad. Sci.* **102**, 15343–15346 (2005).

5. Chapman, H. N. *et al.* High-resolution ab initio three-dimensional x-ray diffraction microscopy. *J. Opt. Soc. Am. A* **23**, 1179–1200 (2006).

6. Whitehead, L. W. *et al.* Diffractive imaging using partially coherent x rays. *Phys. Rev. Lett.* **103**, 243902 (2009).

7. Williams, G. J., Quiney, H. M., Peele, A. G. & Nugent, K. A. Coherent diffractive imaging and partial coherence. *Phys. Rev. B* **75**, 104102 (2007).

8. Williams, G. J., Pfeifer, M. A., Vartanyants, I. A. & Robinson, I. K. Three-dimensional imaging of microstructure in au nanocrystals. *Phys. Rev. Lett.* **90**, 175501 (2003).

9. Vartanyants, I. & Robinson, I. Partial coherence effects on the imaging of small crystals using coherent x-ray diffraction. *J. Phys.: Condens. Matter* **13**, 10593–10611 (2001).

10. Kneip, S. *et al.* Bright spatially coherent synchrotron x-rays from a table-top source. *Nat Phys* **6**, 980–983 (2010).

11. Huang, W. J., Zuo, J. M., Jiang, B., Kwon, K. W. & Shim, M. Sub-angstrom-resolution diffractive imaging of single nanocrystals. *Nature Physics* **5**, 129–133 (2009).

12. Fienup, J. R. Phase retrieval algorithms - a comparison. *Appl. Opt.* **21**, 2758–2769 (1982).

13. Eisebitt, S. *et al.* Lensless imaging of magnetic nanostructures by x-ray spectro-holography. *Nature* **432**, 885 (2004).

14. Sayre, D. Some implications of a theorem due to shannon. *Acta Crystallogr* **5**, 843 (1952).

15. Abbey, B. *et al.* Keyhole coherent diffractive imaging. *Nature Phys.* **4**, 394–398 (2008).

16. Dierolf, M. *et al.* Ptychographic x-ray computed tomography at the nanoscale. *Nature* **467**, 436–439 (2010).

17. Nugent, K. A. Coherent methods in the x-ray sciences. *Adv. Phys.* **59**, 1–99 (2010).

18. Vartanyants, I. A. & Singer, A. Coherence properties of hard x-ray synchrotron sources and x-ray free-electron lasers. *New journal of physics* **12**, 035004 (2010).

19. Chen, B. *et al.* Multiple wavelength diffractive imaging. *Phys. Rev. A* **79**, 023809 (2009).

20. Abbey, B. *et al.* Lensless imaging using broadband x-ray sources. *Nat Photon* **5**, 420–424 (2011).

21. Bates, R. Fourier phase problems are uniquely solvable in more than one dimension. 1. underlying theory. *Optik (Stuttgart)* **61**, 247–262 (1982).

22. Schell, A. C. A technique for determination of radiation pattern of a partially coherent aperture. *IEEE Transactions of antennas and propagation* **Ap15**, 187 (1967).

23. Nugent, K. A. Partially coherent diffraction patterns and coherence measurement. *J. Opt. Soc. Am. A* **8**, 1574–1579 (1991).

24. Clark, J. N. *et al.* Dynamic sample imaging in coherent diffractive imaging. *Optics letters* **36**, 1954 (2011).

25. Quiney, H. M. & Nugent, K. A. Biomolecular imaging and electronic damage using x-ray free-electron lasers. *Nature Phys.* **7**, 142–146 (2011).

26. Marchesini, S. *et al.* X-ray image reconstruction from a diffraction pattern alone. *Phys. Rev. B* **68**, 140101 (2003).

27. Clark, J. N. *Advances in Fresnel Coherent Diffractive Imaging*. Ph.D. thesis, La Trobe University (2010).

28. Leake, S. J., Newton, M. C., Harder, R. & Robinson, I. K. Longitudinal coherence function in x-ray imaging of crystals. *Opt. Express* **17**, 15853–15859 (2009).

29. Richardson, W. Bayesian-based iterative method of image restoration. *J. Opt. Soc. Am.* **62**, 55 (1972).

30. Lucy, L. Iterative technique for rectification of observed distributions. *Astron. J.* **79**, 745–754 (1974).

Acknowledgements This work was supported by FP7 advanced grant from the European Research Council. The experimental work was carried out at Advanced Photon Source Beamline 34-ID-C, built with funds from the US National Science Foundation under Grant DMR-9724294 and operated by the US Department of Energy, Office of Science, Office of Basic Energy Sciences, under Contract DE-AC02-06CH11357.

Author contributions

Additional information The authors declare no competing financial interests. Correspondence and requests for materials should be addressed to J.N.C. (email: jesse.clark@ucl.ac.uk).

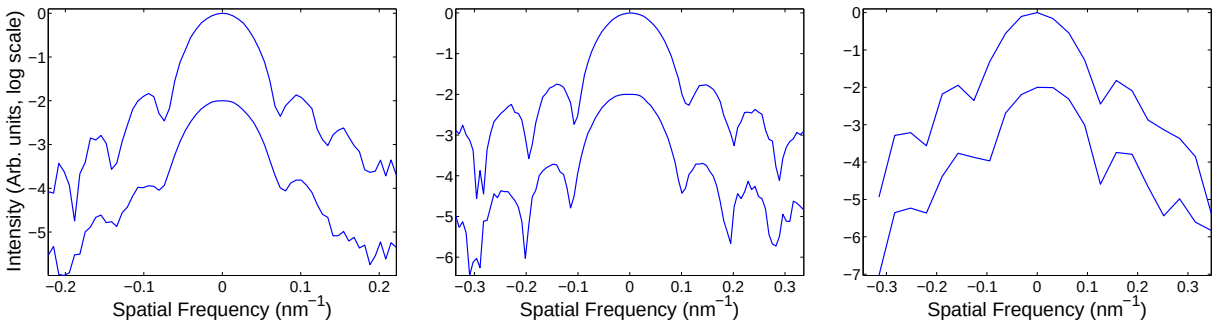

Figure 1: Line-outs through the centre of the diffraction pattern of a gold nanocrystal measured under two coherence conditions. The "high coherence" (top line) and"low coherence" (bottom line) data are displayed on the same plot. From left to right, $I_{pc}(q_x, 0, 0)$,$I_{pc}(0, q_y, 0)$ and $I_{pc}(0, 0, q_z)$. The lower line out has been offset for clarity.

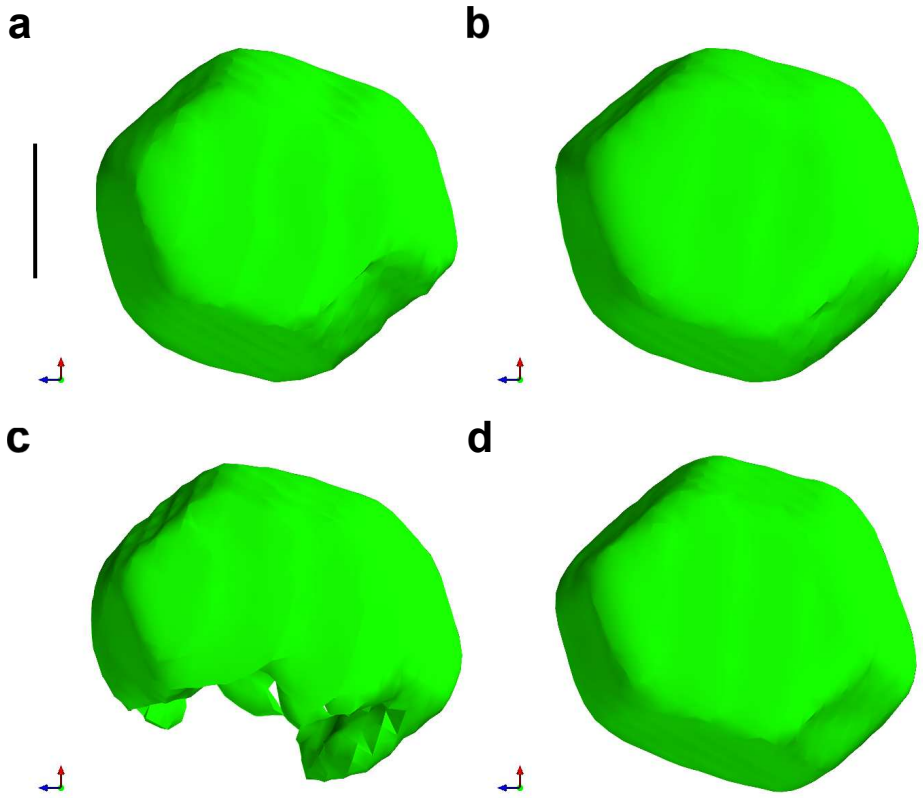

Figure 2: Isosurfaces (50% of the maximum) of the reconstructed nanocrystal for differing coherence conditions. a) Imaged under high coherence conditions assuming full coherence and b) using the partially coherent modulus constraint. Images from the low coherence conditions assuming assuming full coherence (c) and using the partially coherent modulus constraint (d). The viewing plane is $x - z$ and the black scale bar represents 100 nm.

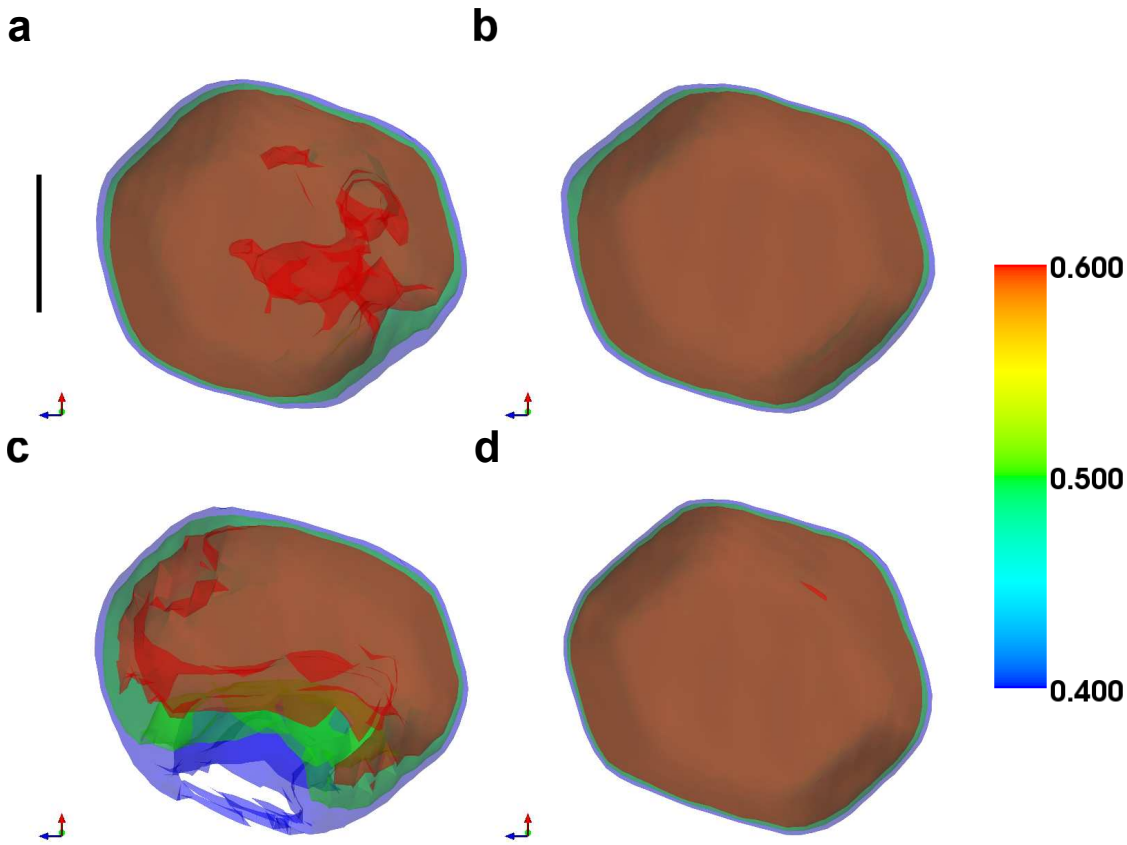

Figure 3: Transparent isosurfaces (40-60% of the maximum) of the reconstructed nanocrystal for differing coherence conditions. a,b Shown is the reconstruction under the high coherence conditions assuming full coherence (a) and using the partially coherent modulus constraint (b). Reconstructions under the low coherence conditions assuming assuming full coherence (c) and using the partially coherent modulus constraint (d). The viewing plane is $x - z$ and the black scale bar represents 100 nm.

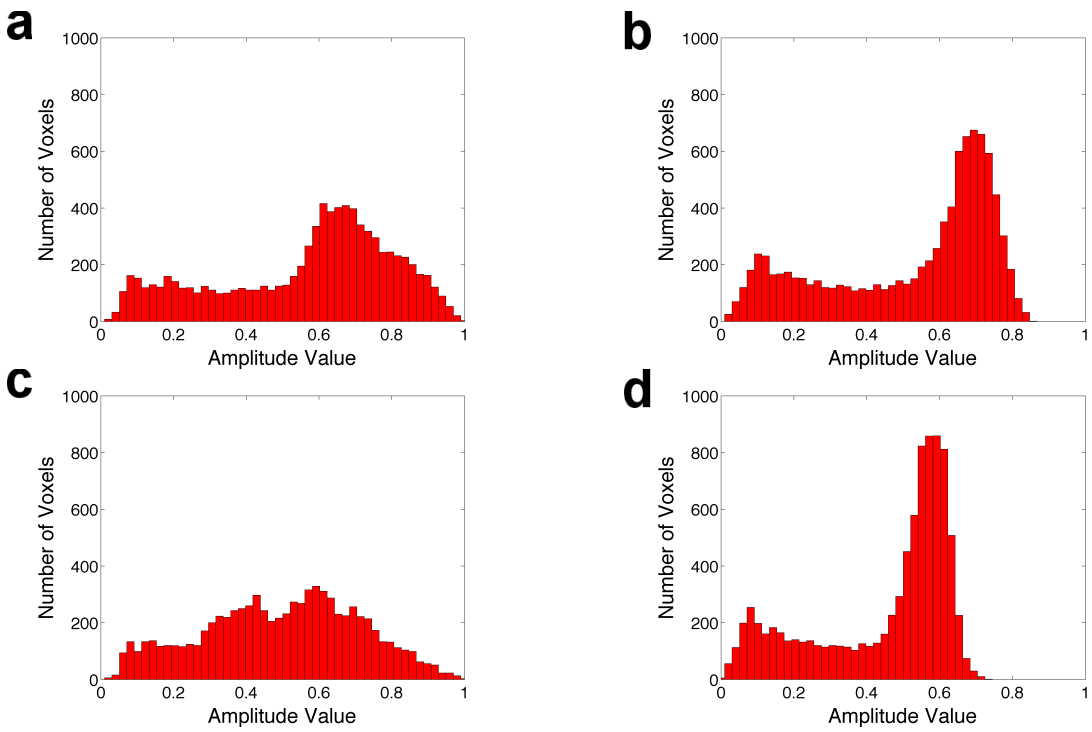

Figure 4: Histograms of amplitude values of pixels within the crystal. The high coherence conditions assuming full coherence (a) and using the partially coherent modulus constraint (b). The histograms for the low coherence reconstructions assuming full coherence (c) and using the partially coherent modulus constraint (d).

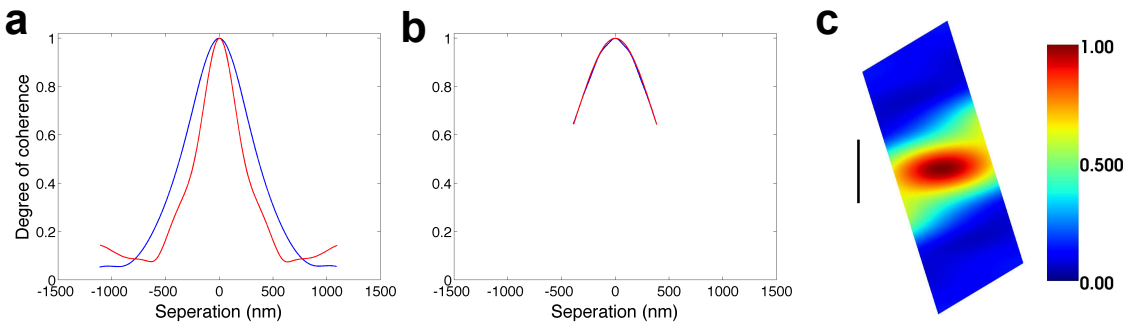

Figure 5: Lineouts through the center of the recovered coherence function in the plane of the sample. Shown is the recovered coherence function for the x (a) and z (b) directions for the high (red line) and low (blue) coherence data sets. Also shown (c) is an $x-z$ slice through the recovered coherence function. The black scale bar represents 500 nm.